

# Characterization of tandem aerosol classifiers for selecting particles: implication for eliminating multiple charging effect

Yao Song<sup>1</sup>, Xiangyu Pei<sup>1</sup>, Huichao Liu<sup>1</sup>, Jijia Zhou<sup>1</sup>, Zhibin Wang<sup>1,2,3\*</sup>

<sup>1</sup>College of Environmental and Resource Sciences, Zhejiang Provincial Key Laboratory of Organic Pollution Process and Control, Zhejiang University, Hangzhou 310058, China

<sup>2</sup>ZJU-Hangzhou Global Scientific and Technological Innovation Center, Hangzhou 311200, China

<sup>3</sup>Key Laboratory of Environment Remediation and Ecological Health, Ministry of Education, Zhejiang University, Hangzhou 310058, China

*Correspondence to:* Zhibin Wang (wangzhibin@zju.edu.cn)

**Abstract.** Accurate particle classification plays a vital role in aerosol studies. Differential mobility analyzer (DMA), centrifugal particle mass analyzer (CPMA) and aerodynamic aerosol classifier (AAC) are commonly used to select particles with a specific mobility diameter, aerodynamic diameter or mass, respectively. However, multiple charging effects cannot be entirely avoided when using either individual techniques or tandem systems such as DMA-CPMA, especially when selecting soot particles with fractal structures. In this study, we calculate the transfer functions of the DMA-CPMA and DMA-AAC in static configurations for flame generated soot particles. We propose an equation that constrains the resolutions of DMA and CPMA to eliminate the multiple charging effect when selecting particles with a certain mass-mobility relationship using the DMA-CPMA system. The equation for the DMA-AAC system is also derived. For DMA-CPMA in a static configuration, our results show that the ability to remove multiply charged particles mainly depends on the particle morphology and resolution settings of the DMA and CPMA. Using measurements from soot experiments and literature data, a general trend in the appearance of multiple charging effect with decreasing size when selecting aspherical particles is observed. As for DMA-AAC in a static configuration, the ability to eliminate particles with multiple charges is mainly related to the resolutions of the classifiers. In most cases, the DMA-AAC in a static configuration can eliminate multiple charging effect regardless of the particle morphology, but multiply charged particles will be selected when decreasing the resolution of the DMA or AAC. We propose that the potential influence of the multiple charging effect should be considered when using the DMA-CPMA or DMA-AAC systems in estimating size- and mass-resolved optical properties in field and lab experiments.

## 1 Introduction

Atmospheric aerosol particles span a wide size range from 1 nm to > 100  $\mu\text{m}$ . A significant size dependence of aerosol physicochemical properties has been widely reported. Particle size can strongly alter the hygroscopic behavior (Biskos et al., 2006), phase state (Cheng et al., 2015) and cloud-nucleating ability

35 (Dusek et al., 2006) of aerosol nanoparticles, indicating the importance of particle size when assessing the  
36 climate effect. Hence, accurate particle classification is essential when investigating the size dependent  
37 behavior of aerosol particles.

38 At present, particles are generally classified by either size or mass in atmospheric aerosol studies. A  
39 differential mobility analyzer (DMA) is the most commonly used size classifier, which selects particles based  
40 on electrical mobility (Knutson and Whitby, 1975; Park et al., 2008; Stolzenburg and McMurry, 2008;  
41 Swietlicki et al., 2008; Wiedensohler et al., 2012). A particle mass analyzer (PMA) includes an aerosol  
42 particle mass analyzer (APM) and a centrifugal particle mass analyzer (CPMA), both of which classify  
43 particles based on their mass-to-charge ratio (Ehara et al., 1996; Olfert and Collings, 2005). The charge  
44 distribution of particles must be known by passing through a neutralizer or similar when classified by DMA  
45 or PMA. However, particles with higher-order charges and identical apparent mobility or mass-to-charge  
46 ratio can be selected simultaneously, which are referred to as the multiple charging effect. This may introduce  
47 uncertainty in the subsequent characterization. Radney et al. (2013) demonstrated that although single-  
48 charged particles account for the highest number fraction (46.3%) of DMA-classified particles (200 nm),  
49 their contributions to the total mass concentration and extinction are insignificant (10.8% and 7.96%,  
50 respectively). Thus, the reported extinction of particles with a certain diameter has been greatly overestimated  
51 due to the multiple charging effect.

52 Previous studies (Shiraiwa et al., 2010; Rissler et al., 2013; Johnson et al., 2014; Johnson et al., 2021) tried to  
53 utilize the combination of size and mass classifiers, such as DMA-APM or DMA-CPMA systems, to obtain  
54 singly charged particles. Theoretically, the ability of a DMA-APM to eliminate multiply charged particles is  
55 governed by the particle morphology and setups of the DMA and APM (Kuwata, 2015). This conclusion  
56 implies that multiply charged particles cannot be effectively excluded for aspherical particles, especially for  
57 soot particles. Radney and Zangmeister (2016) investigated the limitations of a DMA-APM with three types  
58 of particles (polystyrene latex (PSL) spheres, ammonium sulfate (AS) and soot particles). Their results  
59 demonstrated that a DMA-APM can resolve multiply charged particles for spherical particles (PSL and AS  
60 particles), but it failed for aspherical soot particles. Multiply charged soot particles led to over 110% errors  
61 in retrieving the mass specific extinction cross section.

62 In contrast to DMA and PMA, an aerodynamic aerosol classifier (AAC) is a novel instrument that selects the  
63 aerodynamic equivalent diameter of aerosol particles based on their relaxation time. The advantage of  
64 utilizing an AAC is that the charge state of the particles does not need to be known in particle classification  
65 compared with the aforementioned classifiers; hence, multiple charging effects can be avoided (Tavakoli and  
66 Olfert, 2013). However, the selected particles are not monodispersed in mobility diameter when an AAC is  
67 used to select aspherical particles (Kazemimanesh et al., 2022).

68 Morphology information, such as effective density ( $\rho_{\text{eff}}$ ), mass–mobility exponent ( $D_{\text{fm}}$ ) and dynamic shape  
69 factor ( $\chi$ ), can be inferred using tandem DMA-PMA system (Park et al., 2003; Zhang et al., 2008; Rissler et  
70 al., 2013; Pei et al., 2018; Zangmeister et al., 2018), DMA-AAC (Tavakoli and Olfert, 2014) and AAC-  
71 CPMA systems (Kazemimanesh et al., 2022). The derived  $\rho_{\text{eff}}$  and  $\chi$  depend upon the combination of

72 instruments used, while the nonphysical values of  $\chi$  and  $\rho_{\text{eff}}$  for aspherical particles can be determined by the  
73 AAC-APM (Yao et al., 2020) and AAC-CPMA (Kazemimanesh et al., 2022).  
74 The theoretical transfer functions of individual classifiers (DMA, CPMA and AAC) and the DMA-APM  
75 system have been previously discussed (Knutson and Whitby, 1975; Ehara et al., 1996; Olfert and Collings,  
76 2005; Stolzenburg and McMurry, 2008; Tavakoli and Olfert, 2013). In this study, we focus on a DMA-  
77 CPMA and DMA-AAC in static configurations to eliminate multiply charged particles. The DMA-CPMA  
78 and DMA-AAC systems mentioned below refer to the tandems of a DMA and CPMA or a DMA and AAC  
79 in a static configuration, respectively. We calculate the transfer functions of the DMA-AAC and DMA-  
80 CPMA systematically. Combined with soot experiments, we demonstrate that multiple charging effects may  
81 still exist after DMA-CPMA classification when selecting aspherical particles and evaluate the light  
82 absorption of selected particles with different charging states using Mie theory. Furthermore, we propose  
83 operating conditions for the DMA-CPMA and DMA-AAC to eliminate multiply charged particles in future  
84 studies. Our results suggest that the size- and mass-resolved optical properties may be overestimated for  
85 small soot particles when using the DMA-CPMA system, which will lower the prediction accuracy of the  
86 fresh soot climate effect. In Sect. 3.1, we calculate the transfer functions of the DMA-CPMA and DMA-  
87 AAC utilizing the literature data of soot particles from Pei et al. (2018). In Sect. 3.2, we measure the multiple  
88 charging effect of the DMA-CPMA using laboratory-generated soot particles, and the bias of optical  
89 measurement induced by multiply charged particles is evaluated in Sect. 3.3.

## 90 **2 Theory and experiment**

### 91 **2.1 Transfer function for individual aerosol classifiers**

#### 92 **DMA**

93 The DMA, consisting of two coaxial electrodes, classifies particles based upon electrical mobility  $Z_p$   
94 (Knutson and Whitby, 1975), which can be calculated as follows:

$$95 \quad Z_p = qB = \frac{neCc(d_m)}{3\pi\mu d_m}, \quad (1)$$

96 where  $q$  is the particle charge,  $n$  is the number of elementary charges,  $B$  is the mobility of the particle,  $e$  is  
97 the elementary charge,  $\mu$  is the viscosity of air, and  $Cc(d_p)$  is the Cunningham slip correction factor. When  
98 the aerosol inlet flow rate equals the aerosol sampling outlet flow rate, the centroid mobility,  $Z_p^*$ , selected by  
99 the DMA is defined as

$$100 \quad Z_p^* = \frac{Q_{\text{sh}}}{2\pi V_{\text{DMA}} L_{\text{DMA}}} \ln\left(\frac{r_{2\_DMA}}{r_{1\_DMA}}\right), \quad (2)$$

101 where  $Q_{\text{sh}}$  is the sheath flow rate,  $V_{\text{DMA}}$  is the voltage between the two electrodes,  $L_{\text{DMA}}$  is the length of the  
102 DMA, and  $r_{1\_DMA}$  and  $r_{2\_DMA}$  are the inner and outer radii of the DMA electrodes, respectively. Assuming  
103 that the aerosol inlet and aerosol sampling flow rates are equal, the transfer function of the DMA can be  
104 expressed as follows when particle diffusion is negligible (Knutson and Whitby, 1975; Stolzenburg and  
105 McMurry, 2008):

$$\Omega(\tilde{Z}_p, \beta_{\text{DMA}}) = \frac{1}{2\beta_{\text{DMA}}} [|\tilde{Z}_p - (1 + \beta_{\text{DMA}})| + |\tilde{Z}_p - (1 - \beta_{\text{DMA}})| - 2|\tilde{Z}_p - 1|], \quad (3)$$

where,  $\tilde{Z}_p = Z_p/Z_p^*$ ,  $\beta_{\text{DMA}}=Q_a/Q_{\text{sh}}$ , and  $Q_a$  is the sample flow rate. The limiting electrical mobilities that DMA can select are  $(1 \pm \beta_{\text{DMA}}) \cdot Z_p^*$ . The maximum and minimum values of  $d_m$  for particles with  $n$  charges can be derived combining  $(1 \pm \beta_{\text{DMA}}) \cdot Z_p^*$  and Eq. (1), and denote as  $d_{m,\text{max}}$  and  $d_{m,\text{min}}$ , respectively. The transfer function is an isosceles triangle with value of 1 at  $Z_p^*$  and going to 0 at  $(1 \pm \beta_{\text{DMA}}) \cdot Z_p^*$ . It translates to asymmetry in  $d_m$  since the relationship between  $d_m$  and  $Z_p$  is nonlinear.

## 112 CPMA

113 The APM consists of two coaxial electrodes which are rotating at an equal angular velocity and a voltage is  
 114 applied between these electrodes to create an electrostatic field (Ehara et al., 1996). The construction of the  
 115 CPMA is similar to the APM, but its inner cylinder rotates faster than the outer cylinder to create a stable  
 116 system of forces (Olfert and Collings, 2005). In the CPMA, the equation of particle motion is expressed as

$$117 \frac{m}{\tau} \frac{dr}{dt} = \frac{mv_{\theta}(r)^2}{r} - \frac{qV_{\text{CPMA}}}{r \ln\left(\frac{r_{2\_CPMA}}{r_{1\_CPMA}}\right)}, \quad (4)$$

118 and the trajectory equation is

$$119 \frac{dr}{dz} = \frac{dr}{dt} \left(\frac{dz}{dt}\right)^{-1} = \frac{c_r}{v_z}, \quad (5)$$

120 where  $\tau$  is the relaxation time,  $m$  is the mass of the particle,  $t$  is time,  $V$  is the voltage difference between the  
 121 two electrodes, and  $r_{1\_CPMA}$  and  $r_{2\_CPMA}$  are the radii of the inner and outer electrodes, respectively.  $c_r$  is the  
 122 particle migration velocity,  $v_z$  is the axial flow distribution and  $v_{\theta}$  is the velocity profile in the angular  
 123 direction,

$$124 v_{\theta} = \omega_1 \frac{\hat{r}^2 - \hat{\omega}}{\hat{r}^2 - 1} r + \omega_1 r_{1\_CPMA}^2 \frac{\hat{\omega} - 1}{\hat{r}^2 - 1} \frac{1}{r} = \alpha r + \frac{\beta}{r}, \quad (6)$$

125 where  $\hat{\omega} = \omega_2/\omega_1$  is the ratio of the rotational speed of the outer electrode to the inner electrode and  $\omega_1$  and  
 126  $\omega_2$  are the rotational speeds of the inner and outer electrodes, respectively.  $\hat{r}$  is the ratio of the inner and outer  
 127 radii.  $\alpha$  and  $\beta$  are the azimuthal flow velocity distribution parameters.

128 Sipkens et al. (2019) presented methods to calculate the transfer function of the CPMA. They considered the  
 129 Taylor series expansion about the center of the gap ( $r_c=(r_{2\_CPMA}+r_{1\_CPMA})/2$ ) instead of the equilibrium radius  
 130 to avoid problems with the scenario in which the equilibrium radius does not exist. This method is much  
 131 simpler and more robust. In this case, the particle migration velocity in the radial direction is

$$132 c_r \approx C_3 + C_4(r - r_c), \quad (7)$$

133 where

$$134 C_3 = \tau \left( \alpha^2 r_c + \frac{2\alpha\beta}{r_c} + \frac{\beta^2}{r_c^3} - \frac{C_0}{mr_c} \right), \quad (8)$$

$$135 C_4 = \tau \left( \alpha^2 - \frac{2\alpha\beta}{r_c} - \frac{3\beta^2}{r_c^3} + \frac{C_0}{mr_c^2} \right), \quad (9)$$

$$136 C_0 = \frac{qV_{\text{CPMA}}}{\ln(r_{2\_CPMA}/r_{1\_CPMA})}, \quad (10)$$

137 Assuming plug flow, the transfer function would be

$$138 \Omega = \frac{r_b - r_a}{2\delta}, \quad (11)$$

139 where  $\delta=(r_{2\_CPMA}-r_{1\_CPMA})/2$  is the half width of the gap between the two electrodes, and

$$140 \quad r_a = \min \left\{ r_{2\_CPMA}, \max \{ r_{1\_CPMA}, G_0(r_{1\_CPMA}) \} \right\}, \quad (12)$$

$$141 \quad r_b = \min \left\{ r_{2\_CPMA}, \max \{ r_{1\_CPMA}, G_0(r_{2\_CPMA}) \} \right\}, \quad (13)$$

$$142 \quad G_0(r_L) = r_c + \left( r_L - r_c + \frac{C_3}{C_4} \right) \exp(-C_4 L \bar{v}) - \frac{C_3}{C_4}, \quad (14)$$

143 where  $G_0(r)$  is the operator used to map the final radial position of the particle to its position at the inlet and  
 144  $\bar{v}$  is the average flow velocity.  $\min\{\}$  and  $\max\{\}$  are the minimum and maximum values of the quantities in  
 145 the brackets, respectively.

146 Reavell et al. (2011) calculated the resolution of the CPMA assuming that the gap between two electrodes is  
 147 narrow enough that the variation of force in the gap can be ignored. The mass resolution ( $R_m$ ) of CPMA is  
 148 related to particles mobility. When selecting the particles with mass of  $m_1$  and mobility of  $B_1$ , the  $R_m$  can be  
 149 calculated by

$$150 \quad R_m = \frac{2\pi B_1 L_{CPMA} r_c^2 \omega^2 m_1}{Q_{CPMA}}, \quad (15)$$

151 where  $\omega$  is the equivalent rotational speed calculated by  $\omega = \alpha + \frac{\beta}{r_c^2}$ ,  $m_1$  is the nominal mass that the CPMA

152 can select,  $Q_{CPMA}$  is the volumetric flow rate. The limiting mass can be calculated by

$$153 \quad m_{n,\min}^{n,\max} = n \cdot m_1 \pm \frac{Q_{CPMA}}{2\pi B_{n,\min}^{n,\max} L_{CPMA} r_c^2 \omega^2} = n \cdot m_1 \pm \frac{m_1}{R_m} \cdot \frac{B_1}{B_{n,\min}^{n,\max}}, \quad (16)$$

154 where  $m_{n,\min}^{n,\max}$  and  $B_{n,\min}^{n,\max}$  are the maximum and minimum mass and corresponding mobility of particles  
 155 bearing number of elementary charges of  $n$  that the CPMA can select, respectively. Further details can be  
 156 found in Reavell et al. (2011) and Sipkens et al. (2019).

### 157 AAC

158 The AAC classifies particles based on relaxation time, which is defined by

$$159 \quad \tau = Bm = \frac{Cc(d_{ae})\rho_0 d_{ae}^2}{18\mu}, \quad (17)$$

160 where  $\mu$  is the viscosity of air.  $Cc(d_{ae})$  is the slip correction factor.  $\rho_0$  is the standard density with a value of 1  
 161 g/cm<sup>3</sup> (Johnson et al. 2018). When the aerosol inlet flow rate equals the aerosol sampling outlet flow rate,  
 162 the transfer function of the AAC can be expressed as (Tavakoli and Olfert, 2013)

$$163 \quad \Omega = \frac{1}{2\beta_{AAC}} [|\tilde{\tau} - (1 - \beta_{AAC})| + |\tilde{\tau} - (1 + \beta_{AAC})| - 2|\tilde{\tau} - 1|], \quad (18)$$

164  $\tau^*$  is the nominal relaxation time, which is classified by the AAC,

$$165 \quad \tau^* = \frac{2Q_{sh}}{\pi\omega^2(r_{1\_AAC}+r_{2\_AAC})^2L}, \quad (19)$$

166 where  $\beta_{AAC} = \frac{Q_a}{Q_{sh}}$ ,  $\tilde{\tau} = \frac{\tau}{\tau^*}$ ,  $r_{1\_AAC}$  and  $r_{2\_AAC}$  are the inner and outer radii of the AAC, respectively. The  
 167 limiting  $\tau$  that AAC can select are  $(1 \pm \beta_{AAC}) \cdot \tau^*$ . The maximum and minimum values of  $d_{ae}$  can be derived  
 168 and denoted as  $d_{ae,\max}$  and  $d_{ae,\min}$ , respectively.

169 **2.2 Experimental setup**

170 A schematic of the experimental setup is illustrated in Fig. 1. Soot particles were generated by a miniature  
 171 inverted soot generator (Argonaut Scientific Ltd., Canada) with a propane flow of 74.8 SCPM (standard mL  
 172 per minute, flow in mL min<sup>-1</sup> converted from ambient to T =298.15 K and P = 101.325 kPa) and an air flow  
 173 rate of 12 SLPM (Standard L per minute, flow in L min<sup>-1</sup> converted from ambient to T =298.15 K and P =  
 174 101.325 kPa). Although this operation setting is not in the open-tip flame regime, the flame is open-tip  
 175 consistent with Fig. 2d in Moallemi et al. (2019). Detailed aerosol generation methods can be found in  
 176 Kazemimanesh et al. (2019b) and Moallemi et al. (2019). The polydispersed aerosols were dried to a relative  
 177 humidity of <20% by a silica dryer and then passed through a soft X-ray neutralizer (Model 3088, TSI, Inc.,  
 178 USA). Five mobility diameters (80 nm, 100 nm, 150 nm, 200 nm and 250 nm) of soot particles were selected  
 179 with the DMA (Model 3081, TSI Inc., USA,  $\beta_{DMA} = 10$ ). For the soot characterization, the mobility-selected  
 180 aerosol flow was switched between two parallel lines and fed into the CPMA (Cambustion Ltd., UK) and  
 181 AAC (Cambustion, Ltd., UK,  $\beta_{AAC} = 10$ ); meanwhile, the condensation particle counter (CPC, Model 3756,  
 182 TSI, Inc., USA, 0.3 L min<sup>-1</sup>) was switched between the CPMA and AAC. The distributions of particle number  
 183 concentration as a function of particle mass ( $m$ ) and aerodynamic diameter ( $d_{ae}$ ) were measured by the  
 184 scanning mode of the CPMA and AAC, respectively, while the CPC recorded their corresponding number  
 185 concentrations at each setpoint. For each  $d_m$ , the  $m$  and  $d_{ae}$  distributions were measured three times. Between  
 186 measurements of each  $d_m$ , the CPC was used behind the DMA, and the number size distribution of the  
 187 generated soot particles was measured by a scanning mobility particle sizer (SMPS) to ensure the number  
 188 size distribution of generated soot particles did not change during the whole experiment. The  $m$  and  $d_{ae}$   
 189 distributions were fitted to log-normal distributions; thus, the modal values denoted as  $m_c$  and  $d_{ae,c}$  for the  
 190 mobility-selected particles were determined. The equation of log-normal distribution used in this study is  
 191 expressed as

$$192 \begin{cases} N(m) = \frac{N_0}{\sqrt{2\pi}\ln\sigma_m} \exp\left(\frac{-(\log(m)-\log(m_c))^2}{2(\ln\sigma_m)^2}\right) \\ N(d_{ae}) = \frac{N_0}{\sqrt{2\pi}\ln\sigma_{ae}} \exp\left(\frac{-(\log(d_{ae})-\log(d_{ae,c}))^2}{2(\ln\sigma_{ae})^2}\right) \end{cases}, \quad (20)$$

193 where  $\sigma_m$  and  $\sigma_{ae}$  are the geometric standard deviations of  $m$  and  $d_{ae}$  distributions, respectively.  $m_c$  and  $d_{ae,c}$   
 194 are the geometric mean of  $m$  and  $d_{ae}$ , respectively.

195 The CPMA and AAC were calibrated with certified PSL spheres (Thermo, USA) with sizes of 70 nm, 150  
 196 nm and 303 nm before the measurement. The measured  $m$  and  $d_{ae}$  were compared to  $m_{PSL}$  and  $d_{ae,PSL}$ , which  
 197 were calculated with the nominal diameter and density of PSL (1050 kg m<sup>-3</sup>). The deviations between  
 198 measured  $m$  and  $m_{PSL}$  or measured  $d_{ae}$  and  $d_{ae,PSL}$  were 2.75% and 5.14%, respectively. To quantify the  
 199 multiple charging effect of particles selected by the DMA-CPMA system, the soot particles were initially  
 200 selected by the DMA-CPMA at different  $d_m$  and the corresponding  $m$ . Then, the  $d_{ae}$  distribution of mobility  
 201 and mass selected particles was obtained by stepping the AAC rotation speed of the cylinder with  
 202 simultaneous measurement of the particle concentration at the AAC outlet using a CPC (Fig. 1b).

## 203 3 Results and discussion

### 204 3.1 Transfer function of the tandem system

205 The DMA, PMA and AAC select particles based on the electrical mobility diameter, mass and aerodynamic  
206 diameter, respectively. These properties can be connected as follows (Decarlo et al. 2004):

$$207 \frac{Cc(d_{ae})\rho_0 d_{ae}^2}{6} = \frac{Cc(d_m)\rho_{eff}d_m^2}{6} = m \frac{Cc(d_m)}{\pi d_m}, \quad (21)$$

208 where  $\rho_{eff} = \frac{6m}{\pi d_m^3}$ . The transfer function of the DMA-APM has been well documented and can be found in

209 Kuwata (2015). The convolution of the transfer functions of the DMA-CPMA and DMA-AAC were  
210 calculated by the following equations.

$$211 \Phi_{DMA-CPMA} = \Omega_{CPMA}\Omega_{DMA}, \quad (22)$$

$$212 \Phi_{DMA-AAC} = \Omega_{DMA}\Omega_{AAC}, \quad (23)$$

213 where  $\Phi$  and  $\Omega$  are the transfer functions of the combined and individual classification systems expressed by  
214 subscripts, respectively. In the following discussion, we explain the transfer functions of the DMA-CPMA  
215 and DMA-AAC utilizing the literature data of soot particles (Pei et al., 2018). The  $d_m$  and  $m$  of the  
216 representative particles are 100 nm and 0.33 fg, respectively, and the corresponding  $d_{ae}$  is 68.3 nm according  
217 to Eq. (21). In the calculation, the following parameter set was employed:  $d_m = 100$  nm,  $Q_{DMA} = 0.3$  L min<sup>-1</sup>,  
218  $\beta_{DMA} = 0.1$ ,  $m = 0.33$  fg,  $Q_{CPMA} = 0.3$  L min<sup>-1</sup>,  $R_m = 8$ ,  $d_{ae} = 68.3$  nm,  $Q_{AAC} = 0.3$  L min<sup>-1</sup>,  $\beta_{AAC} = 0.1$ . The  
219 transfer functions of DMA-CPMA and DMA-AAC were solved iteratively using logarithmically spaced  $d_m$ ,  
220  $m$  and  $d_{ae}$ , which included 600 points each. The ranges of  $d_m$ ,  $m$  and  $d_{ae}$  used in the calculations were from  
221 0.8 times  $d_{m1,min}$  to 1.2 times  $d_{m2,max}$ , and from 0.8 times  $m_{1,min}$  to 1.2 times  $m_{2,max}$ , from 0.8 times  $d_{ae,min}$  to 1.2  
222 times  $d_{ae,max}$ , respectively. The dimensions of the individual classifiers are summarized in Table 1.

#### 223 DMA-CPMA

224 The DMA-CPMA transfer function ( $\Phi_{DMA-CPMA}$ ) for particles mentioned above, i.e., particles with  $d_m$  of 100  
225 nm and  $m$  of 0.33 fg, is calculated in  $\log(d_m)$ - $\log(m)$  space, as shown in Fig. 2. The particles are shown in  
226 Fig. 2 in actual  $d_m$  and  $m$ , but when we calculate the resolution of DMA and CPMA, the mobility and effective  
227 mass are used. The resolution of CPMA can be calculated by Eq. (15), where  $m_1$  is the mass of singly charged  
228 particles which can be selected by the CPMA, i.e., effective mass. In  $\log(d_m)$ - $\log(m)$  space, the mass–mobility  
229 relationship is

$$230 (m/\text{fg}) = k_f (d_m/\text{nm})^{D_{fm}}, \quad (24)$$

$$231 \log(m/\text{fg}) = D_{fm} \log(d_m/\text{nm}) + \log(k_f), \quad (25)$$

232 In general,  $D_{fm}$  equals 3 for spherical particles and smaller than 3 for aspherical particles, although  $D_{fm}$  can  
233 be larger than 3 for particles that are non-spherical at small  $d_m$  and approach spherical as  $d_m$  increases. In the  
234  $\log(d_m)$ - $\log(m)$  space, the relationship of  $m$  and  $d_m$  is linear, with the slope expressed as the mass–mobility  
235 exponent ( $D_{fm}$ ) and the intercept representing the pre-exponential factor ( $k_f$ ). Under this specific operation  
236 condition, no overlap was observed between the spherical particle population (black line) and the  
237 classification region (the colored blocks) for doubly charged particles, implying that only the singly charged

238 particles were selected. For aspherical particles with  $D_{fm} < 3$ , such as soot particles with aggregate structures,  
 239 the particle population may overlap the doubly charged region when the slope ( $D_{fm}$ ) is small enough; however,  
 240 the combination of DMA and CPMA is generally used to avoid the multiple charge effect in soot studies.  
 241 The reported  $D_{fm}$  values are typically in the range of 2.2–2.4 for fresh soot particles (Rissler et al., 2013) and  
 242 diesel soot particles (Park et al., 2003). In the exemplary case (Pei et al., 2018), the derived  $D_{fm}$  of premixed  
 243 flame-generated soot particles was 2.28, resulting in the particles population always going through the  
 244 transfer area of doubly charged particles. This implies that the performance of the DMA-CPMA to eliminate  
 245 multiply charged particles to a certain extent depends on the particle morphology.

246 The DMA-CPMA system can eliminate the multiply charged particles only if the  $D_{fm}$  of the particles is larger  
 247 than the slope of a line connecting  $(d_m, m) = (d_{m2,min}, m_{2,max})(d_{m1}, m_1)$  (as  $PP_0$  shown in Fig. 2). Since the  
 248 CPMA is used downstream of the DMA,  $m_{2,max}$  at the  $d_m$  of  $d_{m2,min}$  can be calculated using Eq. (16) with the  
 249 known mobility. Accordingly, the ideal condition under static operation to completely eliminate the multiply  
 250 charged particles is

$$251 \quad D_{fm} > PP_0 = \frac{\log(m_{2,max}/m_1)}{\log(d_{m2,min}/d_{m1})} = \frac{\log\left(2 + \frac{2}{R_m(1+\beta_{DMA})}\right)}{\log\left(\frac{2}{(1+\beta_{DMA})} \frac{Cc(d_{m2,min})}{Cc(d_{m1})}\right)} \quad (26)$$

252 The ability of the DMA-CPMA to eliminate multiply charged particles depends on the selected  $d_m$ ,  $m$  and  
 253 resolutions of both the DMA and CPMA. Combining Eq. (15), equation (26) gives instructions in actual  
 254 operation to eliminate multiply charged particles. When selecting particles of certain  $d_m$  and  $m$ , by decreasing  
 255  $Q_{CPMA}$ , or increasing  $\omega$  and  $\beta_{DMA}$ , i.e., by increasing the resolution of the measurement, the potential of  
 256 multiply charged particles is reduced. Thus, the key to evaluating whether there is a multiple charging effect  
 257 lies in the particle morphology ( $D_{fm}$ ) and the slope of  $PP_0$  calculated from Eq. (26) theoretically.

258 In addition to the instrument setup, the particle morphology is also crucial for the DMA-CPMA. Here, we  
 259 simulate the critical slope of  $PP_0$  when selecting different  $d_m$  and  $m$  under the common selecting conditions  
 260 ( $\beta_{DMA} = 0.1$ ,  $Q_{CPMA} = 0.3 \text{ L min}^{-1}$ ,  $R_m = 8$ ) using Eq. (26), which is represented as contour lines in Fig. 3 (A  
 261 black and white version is shown as Fig. S4). Under these selection conditions, the DMA-CPMA can select  
 262 monodispersed particles when the  $D_{fm}$  of the particles is larger than the critical slope of  $PP_0$ . When selecting  
 263 small aspherical particles or particles with extremely low density, the critical slope of  $PP_0$  is relatively higher,  
 264 and the DMA-CPMA classification is sensitive to multiple charging effect. As shown in Fig. 3,  $d_m$ ,  $m$  and  
 265 the corresponding  $D_{fm}$  were taken from the literature (Park et al., 2003; Rissler et al., 2013; Tavakoli et al.,  
 266 2014; Ait Ali Yahia et al., 2017; Dastanpour et al., 2017; Forestieri et al., 2018; Pei et al., 2018;  
 267 Kazemimanesh et al., 2019a). Generally, for soot particles with  $D_{fm}$  of 2.2-2.4, the multiple charging effect  
 268 can be avoided for the DMA-CPMA when selecting soot particles with mobility diameters larger than 200  
 269 nm, while it fails to eliminate multiply charged particles when selecting small soot particles, as shown by the  
 270 circles and squares in Fig. 3. These potential uncertainties are discussed in detail with flame-generated soot  
 271 particles in Sect. 3.2.

## 272 DMA-AAC



273 The advantage of the AAC versus the CPMA is that there is no need for a neutralizer to charge aerosol  
 274 particles to a known charge state. Measuring solely with an AAC will avoid multiple charging. However,  
 275 aspherical particles with different mass can be selected by the AAC as having identical aerodynamic diameter  
 276 ( $d_{ae}$ ) but the  $d_m$  range of this population is wide since soot particles have different densities. Multiple charging  
 277 becomes a problem when the tandem measurement is made with a DMA or PMA. According to Eq. (21) and  
 278 Eq. (24), the relationship of  $d_{ae}$  and  $d_m$  of aspherical particles can be expressed as follows:

$$280 \log(d_{ae}/nm) = \frac{1}{2}(D_{fm} - 1)\log(d_m/nm) + \frac{1}{2}\log\left(\frac{6}{\pi} \frac{Cc(d_m)k_f}{Cc(d_{ae})\rho_0} \cdot 10^9\right), \quad (27)$$

281 which indicates that the relationship between  $d_{ae}$  and  $d_m$  is nonlinear since  $Cc(d_m)$  and  $Cc(d_{ae})$  vary with  $d_m$   
 282 and  $d_{ae}$ , respectively. Particle morphology can be derived from the relationship between  $d_m$  and  $d_{ae}$  measured  
 283 by a DMA and AAC, respectively. To simulate the transfer function of the DMA-AAC, the same particles  
 284 ( $d_m = 100$  nm,  $m = 0.33$  fg,  $D_{fm} = 2.28$ ) as those used in the calculations of the DMA-CPMA were selected.  
 285 The corresponding  $d_{ae}$  was numerically solved using the known mass-mobility relationship. The transfer  
 286 function of the DMA-AAC is shown in  $\log(d_{ae})$ - $\log(d_m)$  (Fig. 4a). In the transfer function of DMA-CPMA,  
 287 the classification regions of singly charged particles and doubly charged particles are on the diagonal. The  
 288 oblique line of particles population is more likely to go through the region of doubly charged particles in the  
 289 transfer function of DMA-CPMA. The transfer functions of singly charged and doubly charged particles are  
 290 in parallel for the DMA-AAC, suggesting that the particles population is less likely to overlap with the region  
 291 of multiply charged particles. Using the example setups ( $d_m = 100$  nm,  $Q_{DMA} = 0.3$  L min<sup>-1</sup>,  $\beta_{DMA} = 0.1$ ,  $d_{ae} =$   
 292  $68.3$  nm,  $Q_{AAC} = 0.3$  L min<sup>-1</sup>,  $\beta_{AAC} = 0.1$ ) of the DMA-AAC, truly monodispersed particles are selected for  
 293 spherical particles and typical soot particles.

294 Similar to the DMA-CPMA system, eliminating multiply charged particles requires that the  $d_{ae,max}$  of the  
 295 AAC at  $d_{m2,min}$  must be smaller than the  $d_{ae}$  of particles of interest, which can be derived from  $d_{m2,min}$  and  $D_{fm}$   
 296 (Eq. (27)),

$$297 d_{ae}(d_{m2,min}, D_{fm}) > d_{ae,max}(d_{m2,min}),$$

$$298 \Rightarrow D_{fm} > \frac{\log(2^{\frac{1+\beta_{AAC}}{1+\beta_{DMA}}})}{\log\left[\frac{2}{1+\beta_{DMA}} \frac{Cc(d_{m2,min})}{Cc(d_{m1})}\right]}, \quad (28)$$

299 This equation describes the minimum value of  $D_{fm}$  to eliminate the multiple charging effect. It is clearly  
 300 shown that the mobility resolution of the DMA and the relaxation time resolution of the AAC determine the  
 301 limiting condition, and the resolution of the AAC is more important compared with the resolution of the  
 302 DMA. The limiting condition is also related to the selected  $d_m$  of the DMA but independent of the selected  
 303  $d_{ae}$  of the AAC (Fig. S1). Setting the same resolutions for the DMA and AAC, particle selection is more  
 304 susceptible to multiple charging effects when selecting small sizes. In Fig. 4a, the values of  $\beta_{DMA}$  and  $\beta_{AAC}$   
 305 are 0.1, resulting in a minimum  $D_{fm}$  of 1.41. This  $D_{fm}$  is smaller than that for most aerosols. Hence, the  
 306 selected particles of the DMA-AAC are truly monodisperse regardless of the particle morphology. However,  
 307 in actual operations, a larger sample flow rate may be required to satisfy the apparatus downstream, while

308 the maximum sheath flow rate of the classifier is restricted by the instrument design (e.g., 30 L min<sup>-1</sup> for the  
309 DMA and 15 L min<sup>-1</sup> for the AAC). In addition, the maximum size ranges are also restricted by the sheath  
310 flow, so in some cases, a lower sheath flow rate is required to select larger particles. When increasing  $\beta_{\text{AAC}}$   
311 to 0.3 (decreasing the resolution of AAC) and leaving  $\beta_{\text{DMA}}$  unchanged, the transfer function becomes broader  
312 (Fig. 4b). The minimum  $D_{\text{fm}}$  is 2.44, which indicates that the multiple charging effect exists for typical soot  
313 particles with  $D_{\text{fm}}$  of 2.2-2.4. The line representing soot particles overlaps with the region of doubly charged  
314 particles. Thus, reducing the resolutions of the DMA or AAC is not suggested in actual operations.

315 We think the transfer functions of DMA-AAC or AAC-DMA are identical regardless of the order of DMA  
316 and AAC. For example, we use AAC-DMA to select particles with  $d_{\text{ae}}$  of 68 nm and  $d_{\text{m}}$  of 100 nm. In Fig.  
317 4a, the transfer function of AAC is the region between the horizontal lines of  $d_{\text{ae,max}}$  (75 nm) and  $d_{\text{ae,min}}$  (63  
318 nm). The soot particles population (red line) goes through this region will be selected by AAC. The mobility  
319 diameter distribution of these relaxation time selected particles is around 80 nm to 120 nm. Then the DMA  
320 is fixed to select particles with  $d_{\text{m}}$  of 100 nm, the particles with double charges and the same mobility ( $d_{\text{m}}$  of  
321 150 nm) have been excluded by AAC. As a result, AAC-DMA select monodispersed particles with  $d_{\text{ae}}$  of  
322 68.3 nm and  $d_{\text{m}}$  of 100 nm. In Fig. 4b, the resolution of AAC is lower and transfer function of AAC is broader  
323 than that in Fig. 4a. The soot particles population (red line) goes through the transfer function region between  
324 the horizontal lines at  $d_{\text{ae}}$  of  $d_{\text{ae,max}}$  (50 nm) and  $d_{\text{ae,min}}$  (86 nm). The mobility diameter distribution of these  
325 relaxation time selected particles is very wide from less than 80 nm to about 158 nm. Then these relaxation  
326 time selected particles were charged and selected by DMA at  $d_{\text{m}}$  of 100 nm, singly charged particles with  $d_{\text{m}}$   
327 of 95 nm~106 nm and doubly charged particles with  $d_{\text{m}}$  of 142 nm~158 nm will be selected.

328 If we use the DMA-AAC, the particles are selected by DMA first. For example, in Fig. 4b, the transfer  
329 function of DMA is shown as two vertical regions which particles with single and double charges can  
330 penetrate. The soot particles (red line) goes through it and two populations of soot particles with mode  $d_{\text{m}}$  of  
331 100 nm and 150 nm will be selected. The corresponding  $d_{\text{ae}}$  distributions of these singly and doubly charged  
332 particles are 66 nm~70 nm and 81 nm~87 nm. These mobility-selected particles are selected at  $d_{\text{ae}}$  of 68.3  
333 nm by AAC and the transfer function of AAC shows that particles with  $d_{\text{ae}}$  of 50 nm~86 nm can penetrate.  
334 As a result, singly charged particles with  $d_{\text{ae}}$  of 66 nm~70 nm and doubly charged particles with  $d_{\text{ae}}$  of 81 nm  
335 ~86 nm can be selected.

336 As a summary, the transfer functions of DMA-AAC and AAC-DMA in a static configuration are the same  
337 no matter the ordering of DMA and AAC.

### 338 **3.2 Evaluation of the multiple charging effect**

339 To quantify the possible biases of the multiple charging effect in the DMA-CPMA system, we conducted a  
340 soot experiment, as demonstrated in Fig. 1. For each mobility-selected particles, the distributions of number  
341 density as a function of  $d_{\text{ae}}$  and  $m$  were determined by the scans. These distributions were then fit to a log-  
342 normal to determine the modal values ( $d_{\text{ae,c}}$ ,  $m_{\text{c}}$ ) and from these values the  $\rho_{\text{eff}}$  were determined. The  
343 uncertainties of  $d_{\text{ae,c}}$  and  $m_{\text{c}}$  were standard deviation of multiple measurements. Representative plots for the

344 measured distributions of  $m$  and  $d_{ae}$  of particles with  $d_m$  of 150 nm and 250 nm are shown in Fig. S2. The  
 345 results are summarized in Table 2. The fitted values of  $D_{fm}$  and  $k_f$  were 2.28 and  $7.49 \times 10^{-6}$  fg, respectively,  
 346 indicating a fractal structure, which is the same as in previous studies (Pei et al., 2018). The effective densities  
 347 of generated soot particles vary from  $>500 \text{ kg m}^{-3}$  at  $d_m = 80 \text{ nm}$  to  $<300 \text{ kg m}^{-3}$  at  $d_m$  of 250 nm determined  
 348 by DMA-CPMA and DMA-AAC. In general, the deviation of values of  $\rho_{eff}$  measured by DMA-CPMA and  
 349 DMA-AAC monotonically decreases with increasing particle size. The deviation is 7.65% for particles of 80  
 350 nm, whereas it decreased to  $<1\%$  for particles larger than 200 nm. The results reveal a strict agreement  
 351 between the two methods for retrieving the particle effective density.

352 According to Fig. 3, the critical slopes of  $PP_0$  for soot particles with  $d_m$  of 80 nm, 100 nm, 150 nm, 200 nm  
 353 and 250 nm are 2.46, 2.41, 2.29, 2.17 and 2.08, respectively. The measured  $D_{fm}$  of 2.28 is smaller than the  
 354 calculated  $PP_0$  for particles with  $d_m$  smaller than 200 nm, which suggests that the contributions from the  
 355 multiply charged particles cannot be eliminated.

356 When selecting particles with  $d_m$  of 80 nm and  $m$  of 0.16 fg, the corresponding DMA-CPMA transfer function  
 357 is shown in Fig. 5a. DMA-CPMA is set to select singly charged particles with  $d_m$  of 80 nm and  $m$  of 0.16 fg,  
 358 while the doubly charged particles with  $d_m$  of 119.3 nm and  $m$  of 0.32 fg will also be selected and the transfer  
 359 function is presented as upper right region. Soot particles curve (red line) goes through the upper-right region  
 360 which doubly charged particle can penetrate ( $d_m$  of 113 nm~118 nm,  $m$  of 0.35 fg~0.39 fg). As a result, we  
 361 conclude that multiple charging effect still exists when DMA-CPMA select soot particles with  $d_m$  of 80 nm  
 362 and  $m$  of 0.16 fg. Since the classification of the AAC is different from the DMA and CPMA, the aerodynamic  
 363 size distributions of mobility- and mass- selected particles were characterized. Fig. 5b shows the particles  
 364 number density aerodynamic size distribution ( $PNSD_{ae}$ ) scanned by the AAC. For each measurement,  
 365  $PNSD_{ae}$  was fitted using log-normal distributions, and three peaks corresponding to singly, doubly and triply  
 366 charged particles were identified. The fractional number concentration of particles with different charging  
 367 state is expressed as follows,

$$368 \quad f_{N,n} = \frac{\int_{d_{ae,low}}^{d_{ae,high}} \frac{dN_n}{d \log(d_{ae})} d \log(d_{ae})}{\sum_{n=1}^3 \int_{d_{ae,low}}^{d_{ae,high}} \frac{dN_n}{d \log(d_{ae})} d \log(d_{ae})}, \quad (29)$$

369 where  $f_{N,n}$  and  $N_n$  are the fractional number concentration and number concentration of particles bearing  $n$   
 370 charges.  $d_{ae,low}$  and  $d_{ae,high}$  denote the minimum and maximum values of  $d_{ae}$  scanned by AAC, respectively.  
 371 The uncertainties are standard deviations of multiple measurements. Some small particles remaining in the  
 372 AAC induced the peak at  $d_{ae} < 40 \text{ nm}$ . These residual particles were measured even if the sample flow was  
 373 filtered. For particles with  $d_m = 80 \text{ nm}$ , the modal  $d_{ae}$  values were 53.9 nm, 60.6 nm and 70.9 nm, and the  
 374 corresponding  $d_{ae}$  values were calculated as 51.5 nm, 62.0 nm and 70.7 nm using Eq. (1) and Eq. (17). The  
 375 experimental results are consistent with the theoretical results with deviations within 5.3%.

376 When selecting particles with  $d_m$  of 200 nm and  $m$  of 1.28 fg, the transfer function is shown in Fig. 6a. The  
 377  $PP_0$  slope of 2.17 is smaller than that  $D_{fm}$  of 2.28, and the generated particles population does not overlap  
 378 with the block of doubly charged particles; thus, the DMA-CPMA classified particles were truly

379 monodispersed.  $\text{PNSD}_{\text{ae}}$  measured by the AAC is unimodal, implying that the classified particles were singly  
380 charged (Fig. 6b).

381 The results of other experiments are shown in Fig. S3. Although the critical slope of  $\text{PP}_0$  when selecting 150  
382 nm particles is close to  $D_{\text{fm}}$  and the transfer function of DMA-CPMA also showed that negligible multiply  
383 charged particles would be selected (Fig. S3d), doubly charged particles were measured in  $\text{PNSD}_{\text{ae}}$  (Fig. S3e).  
384 These doubly charged particles were selected, probably owing to particle diffusion. The nondiffusion models  
385 were used to calculate the transfer function, but the transfer function can be broader because of diffusion. In  
386 summary, for a type of particle with the same mass–mobility relationship, the possibility of multiple charging  
387 increases for small particles when selected by the DMA-CPMA system, which is consistent with the  
388 theoretical calculation in Sect. 3.1.

### 389 3.3 Atmospheric implication

390 The DMA-APM and DMA-CPMA systems are usually adopted to eliminate multiply charged particles in  
391 soot aerosol studies. Although they might fail to select monodispersed particles, downstream measurements  
392 by instruments such as a single-particle soot photometer (SP2) will not be interfered with, which characterizes  
393 the distinct information of a single particle. Nevertheless, for techniques measuring the properties of an entire  
394 aerosol population, e.g., scattering coefficient by a nephelometer or absorption coefficient by a photoacoustic  
395 spectrometer, multiply charged particles can induce significant bias. A previous study (Radney and  
396 Zangmeister, 2016) noted that the DMA-APM failed to resolve multiply charged particles for soot particles  
397 when selecting 150 nm flame-generated particles, which caused a 110% error in extinction measurement. To  
398 investigate the multiple charging effect for DMA-CPMA classification, the optical absorption coefficient of  
399 particles with different charging states after DMA-CPMA classification was calculated from  $\text{PNSD}_{\text{ae}}$ . Mie  
400 theory was used to calculate the theoretical absorption coefficient at a wavelength of 550 nm. Mie theory is  
401 probably not the “best” method to use here since soot particles are aspherical agglomerates. Realistically,  
402 however, the Mie comparison is only being used to prove a point about the impact of multiple charging.  
403 Therefore, in this instance, any errors in the calculated optical properties are somewhat inconsequential. The  
404 refractive index used in the Mie code was  $1.95+0.79i$  (Bond and Bergstrom, 2006). The  $\text{PNSD}_{\text{ae}}$  for different  
405 charging state particles was converted to volume-equivalent diameter size distributions ( $\text{PNSD}_{\text{ve}}$ ), which was  
406 used in Mie theory to determine the absorption coefficient. The method to calculate  $\text{PNSD}_{\text{ve}}$  is described in  
407 Sect. S1. Subsequently, the absorption coefficient,  $\alpha_{\text{abs}}$ , was derived using Mie theory and the  $\text{PNSD}_{\text{ve}}$  of  
408 particles with different charging states. The fractional absorption coefficient for particles with different  
409 charging state is calculated as follows,

$$410 \quad f_{\text{abs},n} = \frac{\int_{d_{\text{ve},\text{low},n}}^{d_{\text{ve},\text{high},n}} \frac{d\alpha_{\text{abs},n}}{d\log(d_{\text{ve}})} d\log(d_{\text{ve}})}{\sum_{i=1}^3 \int_{d_{\text{ve},\text{low},n}}^{d_{\text{ve},\text{high},n}} \frac{dN_n}{d\log(d_{\text{ve}})} d\log(d_{\text{ve}})}, \quad (30)$$

411 where  $f_{\text{abs},n}$  and  $\alpha_{\text{abs},n}$  are the fractional absorption coefficient and absorption coefficient of particles bearing  
412  $n$  charges, respectively.  $d_{\text{ve},\text{low},n}$  and  $d_{\text{ve},\text{high},n}$  denote the minimum and maximum value of  $d_{\text{ve}}$  of particles with  
413  $n$  charges, which are converted from  $d_{\text{ae},\text{low}}$  and  $d_{\text{ae},\text{high}}$  scanned by AAC, respectively.

414 The overestimation of mass absorption cross-section (MAC) is calculated by

$$415 \frac{\Delta \text{MAC}}{\text{MAC}} = \frac{\frac{\alpha_{\text{abs,tot}}}{m_p N_{\text{tot}}} \frac{f_{\text{abs},1} \alpha_{\text{abs,tot}}}{m_p f_{N,1} N_{\text{tot}}}}{\frac{f_{\text{abs},1} \alpha_{\text{abs,tot}}}{m_p f_{N,1} N_{\text{tot}}}} = \frac{f_{N,1}}{f_{\text{abs},1}} - 1, \quad (31)$$

416 where  $\alpha_{\text{abs,tot}}$  and  $N_{\text{tot}}$  is the total absorption coefficient and number concentration of particles selected by  
 417 DMA-CPMA, respectively.  $m_p$  is the actual mass of singly charged particles selected by DMA-CPMA. The  
 418 uncertainties were calculated from propagation of errors. For soot particles with diameters <200 nm, the  
 419 optical absorption contributions of particles with different charging states and the MAC overestimation are  
 420 summarized in Table 3. For soot particles with a diameter of 80 nm, the contributions of particles with  
 421 different charging states are shown in Fig. 5c. Doubly charged particles only account for 26.7%  $\pm$ 3.0% of the  
 422 total number concentration but provide a large fractional contribution to the total absorption (45.7%  $\pm$ 4.2%).  
 423 Additionally, a small fraction (1.1%  $\pm$ 0.4%) of triply charged particles accounted for 3.7%  $\pm$ 1.5% of the  
 424 absorption. As a result, the MAC was overestimated by 42.7%  $\pm$ 9.1%, and the directive radiative force (DRF)  
 425 was overestimated by 42.7%  $\pm$ 9.1%. The DRF was calculated using previous global climate models (Bond et  
 426 al., 2016). For particles selected by the DMA-CPMA at a  $d_m$  of 200 nm and an  $m$  of 1.28 fg, the selected  
 427 particles were truly dispersed, and the measured optical properties were valid (Fig. 6c).

428 A large amount of 70 nm -90 nm soot particles was emitted from diesel engine (Wierzbicka et al., 2014), and  
 429 neglecting the multiple charging effect in the measurement of mass-specific MAC on this size range will  
 430 result in significant bias in the estimation of radiative forcing of automobile-emitted soot particles, which  
 431 may lead to large errors in climate model.

432 According to Table 3, the number fraction of doubly charged particles declines with the size of the nominated  
 433 particles, i.e., 26.7%  $\pm$ 3.0% and 17.6%  $\pm$ 0.5% for 80 nm and 100 nm particles, respectively, but only 4.2%  $\pm$ 1.1%  
 434 for 150 nm particles. Accordingly, the MAC was largely overestimated for 80 nm and 100 nm particles  
 435 (42.7%  $\pm$ 9.1% and 28.0%  $\pm$ 1.8%, respectively) but moderately overestimated for 150 nm particles  
 436 (9.2%  $\pm$ 4.1%). To summarize, our results indicated that the combination of tandem classifiers is not sufficient  
 437 to completely eliminate multiply charged particles when selecting small flame-generated soot particles,  
 438 which introduced noticeable bias for absorption measurements and led to overestimation of the MAC. As a  
 439 result, the DRF of soot particles was also overestimated.

#### 440 **4 Conclusion**

441 In this study, we demonstrate the transfer functions of DMA-CPMA and DMA-AAC and discuss their  
 442 limitations to eliminate multiply charged particles. For aspherical particles, there is no guarantee that the  
 443 multiple charging effect can be avoided in DMA-CPMA or DMA-AAC systems. Usually, a DMA-AAC can  
 444 select truly monodisperse particles, but the method can suffer from multiple charging when decreasing the  
 445 resolutions of the DMA and AAC. The ability of the DMA-CPMA to eliminate multiple charging effect  
 446 mainly depends on the particle morphology and the instrument resolutions. This tandem system is more  
 447 sensitive to multiple charging effect with decreasing  $D_{\text{fm}}$  and decreasing nominal size of particles. The DMA-

448 CPMA failed to eliminate multiply charged particles when selecting soot particles with diameters < 150 nm.  
 449 Although doubly charged particles accounted for a small fraction of the number concentration, they  
 450 contributed most significantly to light absorption, which indicated that multiply charged particles can induce  
 451 an obvious contribution to light absorption and lead to an overestimation of DRF for flame-generated soot  
 452 particles.

453

454 *Code/Data availability.* Code/Data are available upon request.

455 *Author contributions.* ZW determined the main goal of this study. YS and XP designed the methods. YS  
 456 carried them out and prepared the paper with contributions from all coauthors. YS, HL and JZ analyzed the  
 457 optical data.

458 *Competing interests.* The authors declare that they have no conflicts of interest.

459 *Acknowledgments.* The study was supported by the National Natural Science Foundation of China (91844301  
 460 and 41805100). We especially acknowledge useful comments and suggestions on the MATLAB script of the  
 461 CPMA transfer function from Timothy A. Sipkens.

## 462 **Appendix A**

### 463 **A1. Nomenclature**

<b>Parameter</b>	<b>Definition</b>
$B$	Mechanical mobility
$C_c(d_p)$	Cunningham slip correction factor
$c_r$	Particle migration velocity
$d_{ae}$	Aerodynamic equivalent diameter
$d_{ae,c}$	the geometric mean of $d_{ae}$ distribution measured by AAC-CPC
$d_{ae,high}$	The maximum value of $d_{ae}$ scanned by AAC
$d_{ae,low}$	The minimum value of $d_{ae}$ scanned by AAC
$d_{ae,max}$	The maximum $d_{ae}$ of particles that can be selected in AAC classification
$d_{ae,min}$	The minimum $d_{ae}$ of particles that can be selected in AAC classification
$d_m$	Mobility equivalent diameter
$d_{mn,max}$	The maximum $d_m$ of particles with n charges that can be selected in DMA classification
$d_{mn,min}$	The minimum $d_m$ of particles with n charges that can be selected in DMA classification
$d_{ve}$	Volume-equivalence size
$D_{fm}$	Mass-mobility exponent
$e$	Elementary charge

$f_{N,n}$	The fractional number concentration of particles with n charges
$f_{\text{abs},n}$	The fractional absorption coefficient of particles with n charges
$k_f$	Mass-mobility pre-exponential factor
$L$	Length of DMA, CPMA or AAC
$m$	Particle mass
$m_c$	the geometric mean of $m$ distribution measured by CPMA-CPC
$m_{n,\text{max}}$	The maximum $m$ of particles with n charges that can be selected in CPMA classification
$m_{n,\text{min}}$	The minimum $m$ of particles with n charges that can be selected in CPMA classification
$n$	Number of elementary charges on the particle
$N_{\text{tot}}$	The total number concentration of particles selected by DMA-CPMA
PNSD	Particle number size distribution
PNSD <sub>ae</sub>	Particle number aerodynamic size distribution
PNSD <sub>ve</sub>	Particle number volume-equivalent size distribution
$q$	Electrical charge on the particle
$Q_a$	Sample flow rate
$Q_{\text{sh}}$	Sheath flow rate
$Q_{\text{CPMA}}$	The volumetric flow rate in CPMA
$r_a$	Lower initial radial position that passes through the classifier
$r_b$	Upper initial radial position that passes through the classifier
$r_1$	Inner radius
$r_2$	Outer radius
$\hat{r}$	$r_1 / r_2$
$R_m$	Mass resolution of CPMA
$t$	Time
$\bar{v}$	Average flow velocity
$v_z$	Axial flow distribution
$v_\theta$	Velocity profile in the angular direction
$V$	Voltage between the two electrodes of DMA or CPMA
$Z_p$	Electrical mobility
$Z_p^*$	$Z_p$ at the maximum transfer function of DMA
$\tilde{Z}_p$	$Z_p / Z_p^*$
$\alpha \beta$	Azimuthal flow velocity distribution parameter
$\alpha_{\text{abs}}$	Absorption coefficient
$\alpha_{\text{abs,tot}}$	The total absorption coefficient of particles selected by DMA-CPMA
$\beta_{\text{AAC}}$	The ratio of flow rates of aerosol flow and sheath flow of AAC

$\beta_{\text{DMA}}$	The ratio of flow rates of aerosol flow and sheath flow of DMA
$\delta$	Half width of the gap between the two electrodes
$\mu$	Air viscosity
$\rho_0$	Standard density, which equals $1 \text{ kg m}^{-3}$
$\rho_{\text{eff}}$	Effective density
$\sigma_m$	The geometric standard deviation of $m$ distribution
$\sigma_{\text{ac}}$	The geometric standard deviation of $d_{\text{ac}}$ distribution
$\tau$	Relaxation time
$\tau^*$	$\tau$ at the maximum of the transfer function
$\tilde{\tau}$	Dimensionless particle relaxation time, $\tilde{\tau} = \tau/\tau^*$
$\chi$	The dynamic shape factor
$\omega_1$	Rotational speed of the inner electrode
$\omega_2$	Rotational speed of the outer electrode
$\hat{\omega}$	$\omega_1/\omega_2$
$\Omega$	Transfer function

---

## 464 **References**

- 465 Ait Ali Yahia, L., Gehin, E., and Sagot, B.: Application of the The Rmophoretic Annular Precipitator (TRAP)  
466 for the study of soot aggregates morphological influence on their thermophoretic behaviour, *J. Aerosol Sci.*,  
467 113, 40-51, <https://doi.org/10.1016/j.jaerosci.2017.07.018>, 2017.
- 468 Biskos, G., Malinowski, A., Russell, L. M., Buseck, P. R., and Martin, S. T.: Nanosize Effect on the  
469 Deliquescence and the Efflorescence of Sodium Chloride Particles, *Aerosol Sci. Technol.*, 40, 97-106,  
470 <https://doi.org/10.1080/02786820500484396>, 2006.
- 471 Bond, T. C., and Bergstrom, R. W.: Light Absorption by Carbonaceous Particles: An Investigative Review,  
472 *Aerosol Sci. Technol*, 40, 27-67, <https://doi.org/10.1080/02786820500421521>, 2006.
- 473 Bond, T. C., Doherty, S. J., Fahey, D. W., Forster, P. M., Berntsen, T., DeAngelo, B. J., Flanner, M. G., Ghan,  
474 S., Kärcher, B., Koch, D., Kinne, S., Kondo, Y., Quinn, P. K., Sarofim, M. C., Schultz, M. G., Schulz, M.,  
475 Venkataraman, C., Zhang, H., Zhang, S., Bellouin, N., Guttikunda, S. K., Hopke, P. K., Jacobson, M. Z.,  
476 Kaiser, J. W., Klimont, Z., Lohmann, U., Schwarz, J. P., Shindell, D., Storelvmo, T., Warren, S. G., and  
477 Zender, C. S.: Bounding the role of black carbon in the climate system: A scientific assessment, *J. Geophys.*  
478 *Res.: Atmos.: Atmospheres*, 118, 5380-5552, <https://doi.org/10.1002/jgrd.50171>, 2013.
- 479 Cheng, Y., Su, H., Koop, T., Mikhailov, E., and Pöschl, U.: Size dependence of phase transitions in aerosol  
480 nanoparticles, *Nat. Commun.*, 6, <https://doi.org/10.1038/ncomms6923>, 2015.
- 481 Dastanpour, R., Momenimovahed, A., Thomson, K., Olfert, J., and Rogak, S.: Variation of the optical  
482 properties of soot as a function of particle mass, *Carbon*, 124, 201-211,  
483 <https://doi.org/10.1016/j.carbon.2017.07.005>, 2017.



484 Dusek, U., Frank, G. P., Hildebrandt, L., Curtius, J., Schneider, J., Walter, S., Chand, D., Drewnick, F., Hings,  
485 S., Jung, D., Borrmann, S., and Andreae, M. O.: Size Matters More Than Chemistry for Cloud-Nucleating  
486 Ability of Aerosol Particles, *Science*, 312, 1375-1378, <https://doi.org/10.1126/science.1125261>, 2006.

487 Ehara, K., Hagwood, C., and Coakley, K. J.: Novel method to classify aerosol particles according to their  
488 mass-to-charge ratio—Aerosol particle mass analyser, *J. Aerosol Sci*, 27, 217-234,  
489 [https://doi.org/10.1016/0021-8502\(95\)00562-5](https://doi.org/10.1016/0021-8502(95)00562-5), 1996.

490 Johnson, T. J.; Nishida, R. T.; Zhang, X.; Symonds, J. P. R.; Olfert, J. S.; Boies, A. M., Generating an aerosol  
491 of homogeneous, non-spherical particles and measuring their bipolar charge distribution. *J. Aerosol Sci*, 153.  
492 <https://doi.org/10.1016/j.jaerosci.2020.105705>, 2021.

493 Johnson, T. J.; Olfert, J. S.; Cabot, R.; Treacy, C.; Yurteri, C. U.; Dickens, C.; McAughey, J.; Symonds, J. P.  
494 R., Steady-state measurement of the effective particle density of cigarette smoke. *J. Aerosol Sci*, 75, 9-16,  
495 <https://doi.org/10.1016/j.jaerosci.2014.04.006>, 2014.

496 Kazemimanesh, M., Dastanpour, R., Baldelli, A., Moallemi, A., Thomson, K. A., Jefferson, M. A., Johnson,  
497 M. R., Rogak, S. N., and Olfert, J. S.: Size, effective density, morphology, and nano-structure of soot particles  
498 generated from buoyant turbulent diffusion flames, *J. Aerosol Sci.*, 132, 22-31,  
499 <https://doi.org/10.1016/j.jaerosci.2019.03.005>, 2019a.

500 Kazemimanesh, M., Moallemi, A., Thomson, K., Smallwood, G., Lobo, P. and Olfert, J.S.: A novel miniature  
501 inverted-flame burner for the generation of soot nanoparticles. *Aerosol Sci. and Technol.*, 53(2), 184-195,  
502 <https://doi.org/10.1080/02786826.2018.1556774>, 2019b.

503 Kazemimanesh, M., Rahman, M.M., Duca, D., Johnson, T.J., Addad, A., Giannopoulos, G., Focsa, C. and  
504 Boies, A.M.: A comparative study on effective density, shape factor, and volatile mixing of non-spherical  
505 particles using tandem aerodynamic diameter, mobility diameter, and mass measurements. *J. Aerosol Sci.*,  
506 161, 105930, <https://doi.org/10.1016/j.jaerosci.2021.105930>, 2022.

507 Knutson, E. O., and Whitby, K. T.: Aerosol classification by electric mobility: apparatus, theory, and  
508 applications, *J. Aerosol Sci.*, 6, 443-451, [https://doi.org/10.1016/0021-8502\(75\)90060-9](https://doi.org/10.1016/0021-8502(75)90060-9), 1975.

509 Kuwata, M.: Particle Classification by the Tandem Differential Mobility Analyzer–Particle Mass Analyzer  
510 System, *Aerosol Sci. Technol.*, 49, 508-520, <https://doi.org/10.1080/02786826.2015.1045058>, 2015.

511 Moallemi, A.; Kazemimanesh, M.; Corbin, J. C.; Thomson, K.; Smallwood, G.; Olfert, J. S.; Lobo, P.,  
512 Characterization of black carbon particles generated by a propane-fueled miniature inverted soot generator.  
513 *J. Aerosol Sci.*, 135, 46-57, <https://doi.org/10.1016/j.jaerosci.2019.05.004>, 2019.

514 Olfert, J. S., and Collings, N.: New method for particle mass classification—the Couette centrifugal particle  
515 mass analyzer, *J. Aerosol Sci.*, 36, 1338-1352, <https://doi.org/10.1016/j.jaerosci.2005.03.006>, 2005.

516 Park, K., Cao, F., Kittelson, D. B., and McMurry, P. H.: Relationship between Particle Mass and Mobility for  
517 Diesel Exhaust Particles, *Environ. Sci. & Technol.*, 37, 577-583, <https://doi.org/10.1021/es025960v>, 2003.

518 Park, K., Dutcher, D., Emery, M., Pagels, J., Sakurai, H., Scheckman, J., Qian, S., Stolzenburg, M. R., Wang,  
519 X., Yang J., and McMurry P. H.: Tandem Measurements of Aerosol Properties—A Review of Mobility

520 Techniques with Extensions. *Aerosol Sci. and Technol.*, 42, 801-816,  
521 <https://doi.org/10.1080/02786820802339561>, 2008.

522 Pei, X., Hallquist, M., Eriksson, A. C., Pagels, J., Donahue, N. M., Mentel, T., Svenningsson, B., Brune, W.,  
523 and Pathak, R. K.: Morphological transformation of soot: investigation of microphysical processes during  
524 the condensation of sulfuric acid and limonene ozonolysis product vapors, *Atmos. Chem. Phys.*, 18, 9845-  
525 9860, <https://doi.org/10.5194/acp-18-9845-2018>, 2018.

526 Radney, J. G., Ma, X., Gillis, K. A., Zachariah, M. R., Hodges, J. T., and Zangmeister, C. D.: Direct  
527 Measurements of Mass-Specific Optical Cross Sections of Single-Component Aerosol Mixtures, *Anal.*  
528 *Chem.*, 85, 8319-8325, <https://doi.org/10.1021/ac401645y>, 2013.

529 Radney, J. G., and Zangmeister, C. D.: Practical limitations of aerosol separation by a tandem differential  
530 mobility analyzer–aerosol particle mass analyzer, *Aerosol Sci. Technol.*, 50, 160-172,  
531 <https://doi.org/10.1080/02786826.2015.1136733>, 2016.

532 Rissler, J., Messing, M. E., Malik, A. I., Nilsson, P. T., Nordin, E. Z., Bohgard, M., Sanati, M., and Pagels,  
533 J. H.: Effective Density Characterization of Soot Agglomerates from Various Sources and Comparison to  
534 Aggregation Theory, *Aerosol Sci. Technol.*, 47, 792-805, [10.1080/02786826.2013.791381](https://doi.org/10.1080/02786826.2013.791381), 2013.

535 Shiraiwa, M., Kondo, Y., Iwamoto, T., and Kita, K.: Amplification of Light Absorption of Black Carbon by  
536 Organic Coating, *Aerosol Sci. & Technol.*, 44, 46-54, <https://doi.org/10.1080/02786820903357686>, 2010.

537 Sipkens, T. A., Olfert, J. S., and Rogak, S. N.: New approaches to calculate the transfer function of particle  
538 mass analyzers, *Aerosol Sci. Technol.*, 54, 111-127, <https://doi.org/10.1080/02786826.2019.1680794>, 2019.

539 Stolzenburg, M. R., and McMurry, P. H.: Equations Governing Single and Tandem DMA Configurations  
540 and a New Lognormal Approximation to the Transfer Function, *Aerosol Sci. Technol.*, 42, 421-432,  
541 <https://doi.org/10.1080/02786820802157823>, 2008.

542 Swietlicki, E., Hansson, H. C., Hämeri, K., Svenningsson, B., Massling, A., McFiggans, G., McMurry, P. H.,  
543 Pet ä ä T., Tunved, P., Gysel, M., Topping, D., Weingartner, E., Baltensperger, U., Rissler, J., Wiedensohler,  
544 A., and Kulmala, M.: Hygroscopic properties of submicrometer atmospheric aerosol particles measured with  
545 H-TDMA instruments in various environments – a review, *Tellus B*, 60, 432–469,  
546 <https://doi.org/10.1111/j.1600-0889.2008.00350.x>, 2008.

547 Tavakoli, F., and Olfert, J. S.: An Instrument for the Classification of Aerosols by Particle Relaxation Time:  
548 Theoretical Models of the Aerodynamic Aerosol Classifier, *Aerosol Sci. Technol.*, 47, 916-926,  
549 <https://doi.org/10.1080/02786826.2013.802761>, 2013.

550 Tavakoli, F., and Olfert, J. S.: Determination of particle mass, effective density, mass–mobility exponent,  
551 and dynamic shape factor using an aerodynamic aerosol classifier and a differential mobility analyzer in  
552 tandem, *J. Aerosol Sci.*, 75, 35-42, <https://doi.org/10.1016/j.jaerosci.2014.04.010>, 2014.

553 Wiedensohler, A., Birmili, W., Nowak, A., Sonntag, A., Weinhold, K., Merkel, M., Wehner, B., Tuch, T.,  
554 Pfeifer, S., Fiebig, M., Fj ä ä A. M., Asmi, E., Sellegri, K., Depuy, R., Venzac, H., Villani, P., Laj, P., Aalto,  
555 P., Ogren, J. A., Swietlicki, E., Williams, P., Roldin, P., Quincey, P., Hüglin, C., Fierz-Schmidhauser, R.,  
556 Gysel, M., Weingartner, E., Riccobono, F., Santos, S., Gr üning, C., Faloon, K., Beddows, D., Harrison, R.,

557 Monahan, C., Jennings, S. G., O'Dowd, C. D., Marinoni, A., Horn, H.-G., Keck, L., Jiang, J., Scheckman, J.,  
558 McMurry, P. H., Deng, Z., Zhao, C. S., Moerman, M., Henzing, B., de Leeuw, G., Lösschau, G., and Bastian,  
559 S.: Mobility particle size spectrometers: harmonization of technical standards and data structure to facilitate  
560 high quality long-term observations of atmospheric particle number size distributions, *Atmos. Meas. Tech.*,  
561 5, 657–685, <https://doi.org/10.5194/amt-5-657-2012>, 2012.

562 Yao, Q., Asa-Awuku, A., Zangmeister, C. D., and Radney, J. G.: Comparison of three essential sub-  
563 micrometer aerosol measurements: Mass, size and shape, *Aerosol Sci. Technol.*, 1-18,  
564 <https://doi.org/10.1080/02786826.2020.1763248>, 2020.

565 Zangmeister, C. D., You, R., Lunny, E. M., Jacobson, A. E., Okumura, M., Zachariah, M. R., and Radney, J.  
566 G.: Measured in-situ mass absorption spectra for nine forms of highly-absorbing carbonaceous aerosol,  
567 *Carbon*, 136, 85-93, <https://doi.org/10.1016/j.carbon.2018.04.057>, 2018.

568 Zhang, R., Khalizov, A. F., Pagels, J., Zhang, D., Xue, H., and McMurry, P. H.: Variability in morphology,  
569 hygroscopicity, and optical properties of soot aerosols during atmospheric processing, *Proc. Natl. Acad. Sci.*,  
570 105, 10291, <https://doi.org/10.1073/pnas.0804860105>, 2008.

571

572

**Table 1 Dimensions of the three classifiers used for transfer function calculation**

Parameter	DMA	CPMA	AAC
$r_1$ (mm)	9.37	100	43
$r_2$ (mm)	19.61	103	45
L (mm)	44.369	200	210
$\omega_2/\omega_1$	—	0.945	—

573

**Table 2. Mobility diameter, mass, aerodynamic diameter, effective densities calculated by DMA-AAC and DMA-CPMA, and the deviation between them for fresh soot particles in the size range of 80–250 nm**

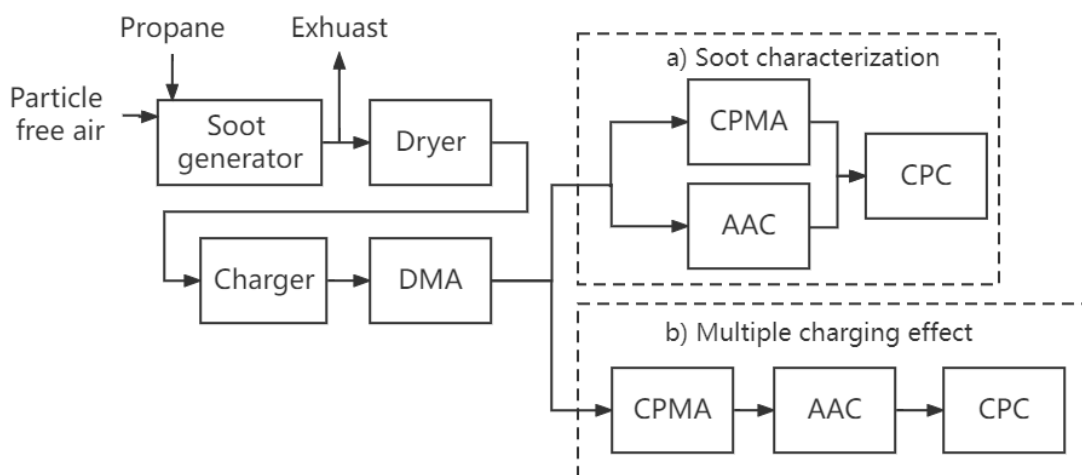
$d_m$ (nm)	$m_c$ (fg)	$d_{ac,c}$ (nm)	$\rho_{DMA-AAC}$ (kg m <sup>-3</sup> )	$\rho_{DMA-CPMA}$ (kg m <sup>-3</sup> )	Deviation
80	0.16±0.01	48.2±0.3	551.2±6.9	596.8±37.30	7.65%
100	0.27±0.01	54.8±0.3	488.0±5.32	515.7±19.10	5.38%
150	0.66±0.07	67.8±0.3	359.1±3.22	373.5±39.61	3.86%
200	1.28±0.10	82.1±0.6	303.2±4.44	305.6±23.87	0.77%
250	2.17±0.16	95.9±0.9	262.8±4.92	265.2±19.56	0.90%

576

**Table 3. Number concentration fractions and absorption contributions for different size fresh soot particles with single, double or triple charges and the overestimation of MAC accordingly**

$d_m$ (nm)	$f_{N,1}$ (%)	$f_{abs,1}$ (%)	$f_{N,2}$ (%)	$f_{abs,2}$ (%)	$f_{N,3}$ (%)	$f_{abs,3}$ (%)	MAC overestimation(%)
80	72.2±2.5	50.6±2.7	26.7±3.0	45.7±4.2	1.1±0.4	3.7±1.5	42.7±9.1
100	82.4±0.5	64.4±0.8	17.6±0.5	35.6±0.8	-	-	28.0±1.8
150	95.8±1.2	87.7±3.1	4.2±1.1	12.3±3.1	-	-	9.2±4.1

579

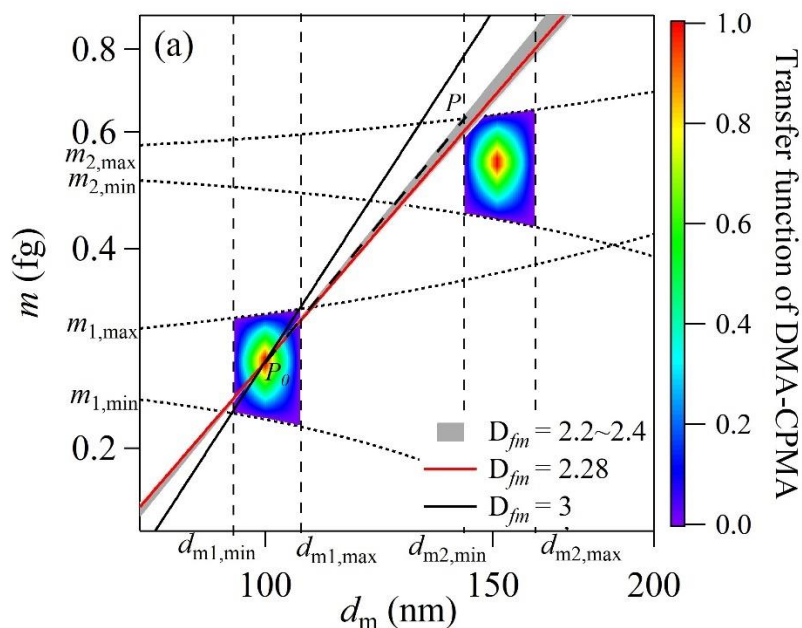


580

**Figure 1: Schematic of the experimental setup: (a) soot characterization and (b) evaluation of multiple charging effects.**

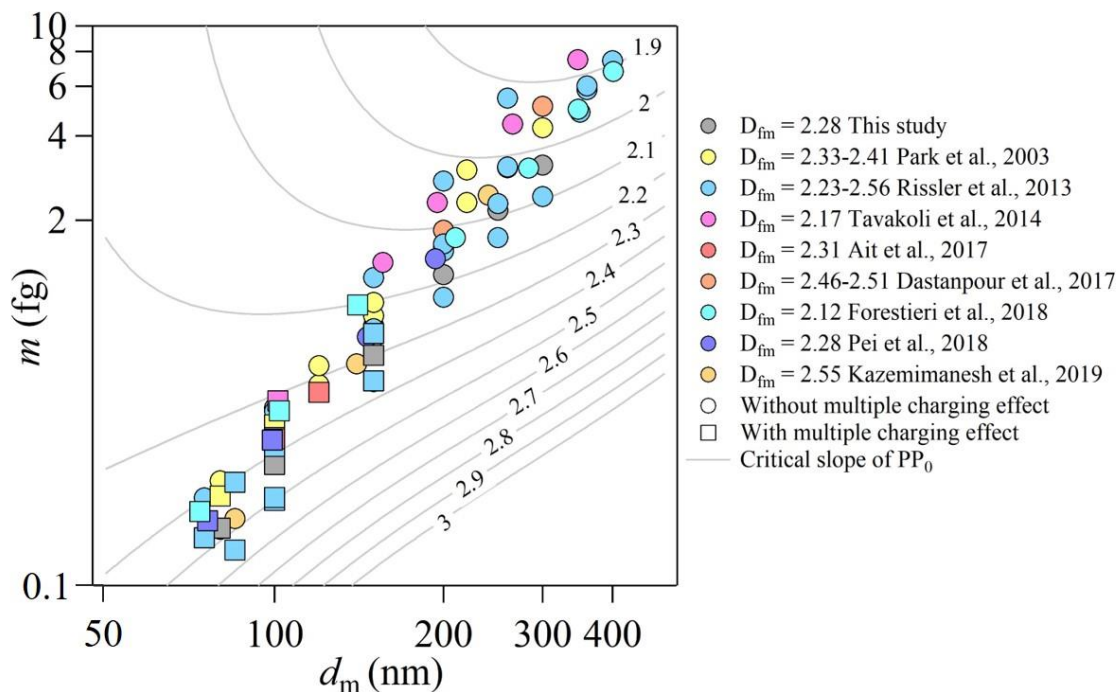
581

582



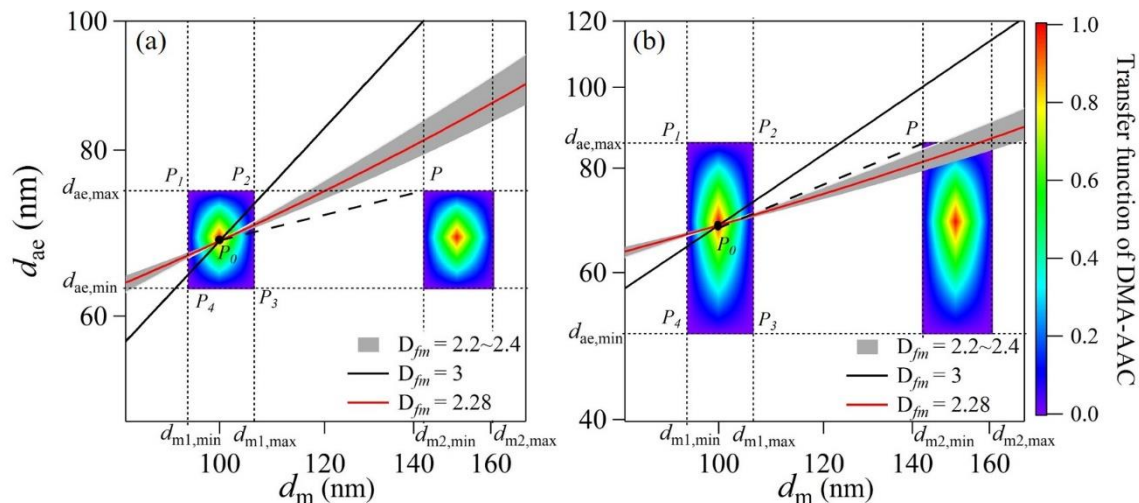
583

584 Figure 2: Example of the DMA-CPMA transfer function of flame-generated soot particles (Pei et al., 2018) in  
 585  $\log(m)\text{-}\log(d_m)$ . The following parameter set was employed for the calculations:  $d_m = 100$  nm,  $\beta_{\text{DMA}} = 0.1$ ,  $m = 0.33$   
 586 fg,  $Q_{\text{CPMA}} = 0.3$  L min<sup>-1</sup>,  $R_m = 8$ . The color blocks are the transfer function of DMA-CPMA, with the rainbow color  
 587 representing the transfer function for singly charged (lower left block) and doubly charged (upper right block)  
 588 particles. The black and red solid lines are particles populations with  $D_{fm}$  values of 3 and 2.28, respectively. The  
 589 gray region is the particle population with  $D_{fm}$  of 2.2-2.4, which is typical for soot aerosols. The dotted lines are  
 590 the limits of  $d_m$  and  $m$  of DMA and CPMA, respectively. The dashed line is the critical slope of  $PP_0$ . The DMA-  
 591 CPMA transfer function for +2 particles does not overlap with the line for spherical particles with a single charge  
 592 ( $D_{fm}=3$ ).



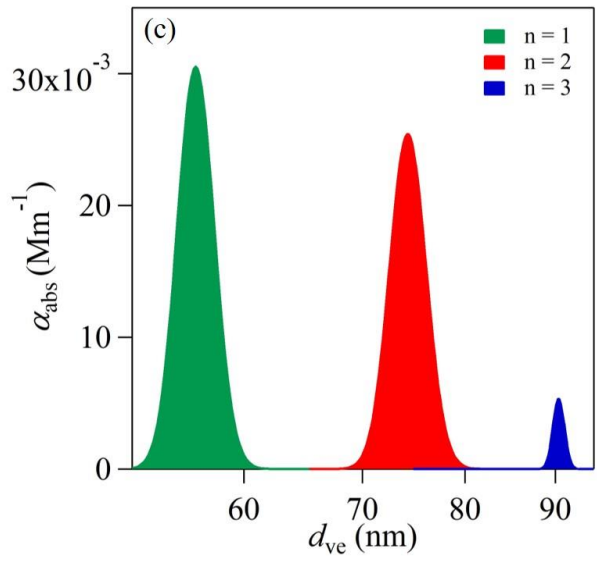
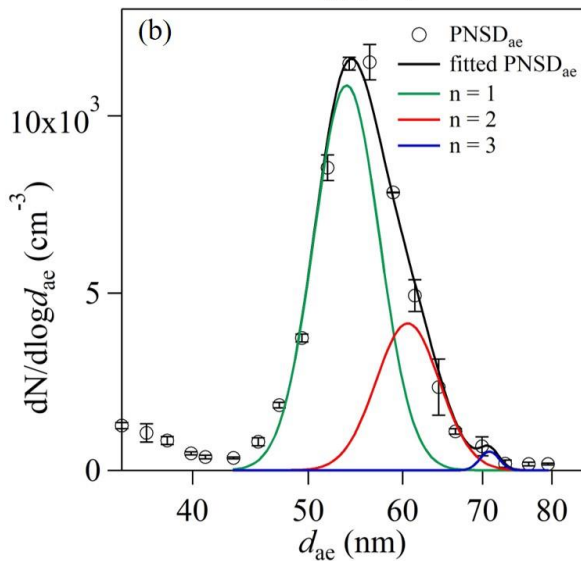
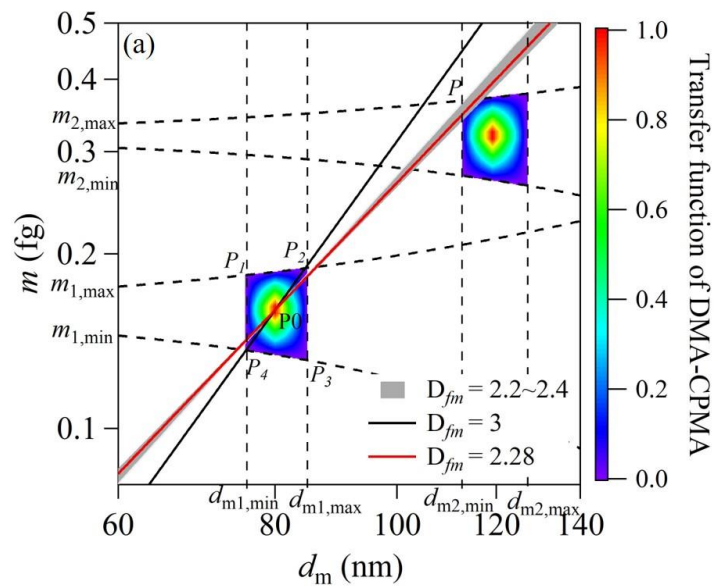
593

594 Figure 3: Variations of the slope of  $PP_0$  as a function of classified  $d_m$  and  $m$ . The following parameter set was  
 595 employed for the calculations:  $\beta_{DMA} = 0.1$ ,  $Q_{CPMA} = 0.3 \text{ L min}^{-1}$ ,  $R_m = 8$ . The contour lines denote the critical slope  
 596 of  $PP_0$ , with values labeled on them. The data points are soot particles measured in the literature (Park et al., 2003;  
 597 Rissler et al., 2013; Tavakoli et al., 2014; Ait Ali Yahia et al., 2017; Dastanpour et al., 2017; Forestieri et al., 2018;  
 598 Pei et al., 2018; Kazemimanesh et al., 2019) and generated in this study (see details in Sect 3.2). The  $D_{fm}$  values of  
 599 these data points are listed in the legend. The data points become square when  $D_{fm}$  is smaller than the critical  
 600 slope of  $PP_0$  in the background, i.e., the potential multiple charging effect may exist.



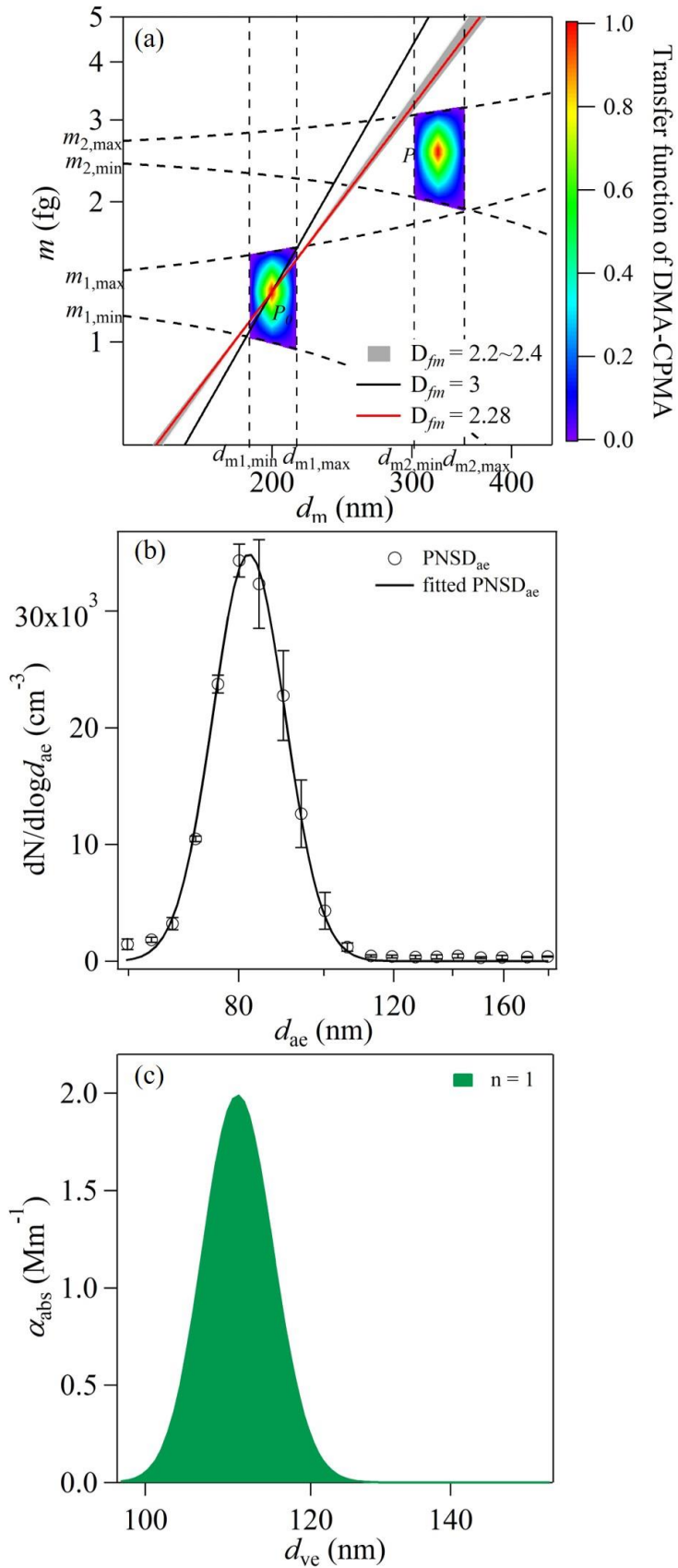
601

602 Figure 4: Examples of transfer function calculation of DMA-AAC of flame-generated soot particles (Pei et al.,  
 603 2018). The following parameter set was employed for the calculations:  $Q_a = 0.3 \text{ L min}^{-1}$ ,  $d_{m1} = 100 \text{ nm}$ ,  $d_{ae} = 68.3$   
 604 nm, (a)  $\beta_{DMA} = 0.1$ ,  $\beta_{AAC} = 0.1$ , (b)  $\beta_{DMA} = 0.1$ ,  $\beta_{AAC} = 0.3$ . The color blocks are the transfer functions of DMA-AAC.  
 605 The black and red solid lines are particle populations with  $D_{fm}$  values of 3 and 2.28, respectively. The gray region  
 606 is the particles population with  $D_{fm}$  of 2.2-2.4, which is typical for soot aerosol. The dashed line is the critical slope  
 607 of  $PP_0$ . The dotted lines are the limiting  $d_m$  and  $d_{ae}$  of DMA and AAC, respectively.



609 **Figure 5: (a) Transfer functions of DMA-CPMA when selecting 80 nm and 0.16 fg particles. The following**  
610 **parameter set was employed for the calculations:  $d_{m1} = 80$  nm,  $\beta_{DMA} = 0.1$ ,  $m_1 = 0.16$  fg,  $Q_{CPMA} = 0.3$  L min<sup>-1</sup>,  $R_m =$**   
611 **8. The red solid line is the generated soot particle population. (b) The aerodynamic size distribution of particles**  
612 **classified by DMA-CPMA. The circles are data measured by AAC-CPC, and the black, green, red and blue lines**  
613 **are log-normal fitted distributions of bulk, singly charged, doubly charged and triply charged particles**  
614 **populations. (c) The contributions to light absorption of particles with single, double and triple charges calculated**  
615 **with Mie theory.**





617 **Figure 6: (a) The transfer functions of DMA-CPMA when selecting 200 nm and 1.28 fg particles. The following**  
618 **parameter set was employed for the calculations:  $d_{m1} = 200$  nm,  $\beta_{DMA} = 0.1$ ,  $m_1 = 1.28$  fg,  $Q_{CPMA} = 0.3$  L min<sup>-1</sup>,  $R_m =$**   
619 **8. The red solid line is the generated soot particle population. (b) The aerodynamic size distribution of particles**  
620 **classified by DMA-CPMA. The circles are data measured by AAC-CPC, and the solid line is the log-normal fitted**  
621 **distribution. (c) Contributions to light absorption of particles with a single charge calculated with Mie theory.**

622